Journal of Membrane Science 683 (2023) 121838

Contents lists available at ScienceDirect

Journal of Membrane Science

journal homepage: www.elsevier.com/locate/memsci

Modifying supersaturation rate with membrane area to volume ratio: Scaling reduction and improved crystal growth control in membrane distillation crystallisation

A. Ouda, Y. Bajón Fernández, E. McAdam *

Cranfield Water Science Institute, Cranfield University, UK

ARTICLE INFO

Keywords:
Scaling mitigation
Zero liquid discharge
Brine
Direct contact
Hollow fibre
NaCl

ABSTRACT

This study provides detailed characterisation of nucleation kinetics, induction time and supersaturation to understand scaling and crystal growth in membrane distillation crystallisation. Membrane area was used to moderate supersaturation rate, as a method to transition across the metastable zone without modifying boundary layer conditions. Increasing membrane area sustained the same water vapour flux but increased supersaturation rate within the crystallising solution (sodium chloride). This reduced induction time and increased the supersaturation level at induction. Membrane scaling was minimised by increasing supersaturation rate despite an increase in nucleation rate. This conforms with classical nucleation theory but contradicts membrane distillation crystallisation literature, where elevated supersaturation is often linked to advanced scaling. The transition from heterogeneous to homogeneous nucleation was evidenced once greater supersaturation at induction was achieved. The probability for scaling within the low supersaturation domain was confirmed through diagnostic investigation of the scaling deposit formed, and the growth mechanism within the scaling layer related to the relevant supersaturation region. Crystal size and morphology were also related to the metastable region, where membrane-to-volume ratio can facilitate higher nucleation rates complemented by greater crystal growth. This study provides critical insight for the development of scaling mitigation strategies and creates a basis for the sustainable design of thermal membrane crystallisation systems.

1. Introduction

Membrane distillation crystallisation (MCr) is a promising technology for resource recovery and the production of high value crystalline products, which can be applied to hypersaline fluids thus affording a potential solution for zero liquid discharge (Q [1,2]. A critical limit to conventional crystallisers is the advent of preferential mixing patterns, which invoke complex local and global mixing phenomenon [3]. This results in poor regulation of supersaturation, which is a critical factor in controlling nucleation and crystal growth [4,5]. The hydrophobic microporous membrane in MCr introduces fixed interfacial area, to deliver fine control over heat and mass transfer mechanisms that yield a uniform evaporation rate, resulting in consistent regulation of supersaturation [6]. This can ensure a final crystal product comprising a fixed size, and narrow size distribution which is of significant value to many prospective end-uses [7–9].

Membrane properties (e.g. polar/non-polar components) have also been acknowledged for their role in adjusting the effective surface free energy (ΔG_s), as this lowers the energy barrier for nucleation through improving solute-membrane interaction [7,10]. Consequently, the hydrophobic membrane can promote heterogeneous nucleation (HEN) through reducing the activation energy (ΔG) to shorten induction time [7]. While this presents a unique advantage to MCr, it also poses a challenge due to the risk of membrane scaling, which reduces control over supersaturation due to the reduction in flux, and could eventually lead to process failure [11–13]. The explicit contribution of the membrane to scaling is not clear but may relate to the solute-membrane interaction extending solute hold-up, or improvement in molecular orientation [7]. It has also been proposed that material morphology can effect scaling as cavity structure [14], roughness and pore structure [11] could lead to solute entrapment, introducing local regions of supersaturation. This may be exacerbated by concentration and temperature polarisation which can alter the concentration, solubility and fluid physics within the primarily laminar boundary layer [15]. Several

* Corresponding author.
E-mail address: e.mcadam@cranfield.ac.uk (E. McAdam).

https://doi.org/10.1016/j.memsci.2023.121838
Received 24 February 2023; Received in revised form 5 June 2023; Accepted 10 June 2023
Available online 10 June 2023
0376-7388/© 2023 The Authors. Published by Elsevier B.V. This is an open access article under the CC BY license (http://creativecommons.org/licenses/by/4.0/).

authors have suggested that with sufficient shear stress, the probability for membrane scaling can be limited by enabling the back transport of crystals from the membrane to the bulk [7,16]. However, this implies that the applied shear stress is sufficient to overcome forces initiated by the solute-membrane interaction, and that the formation of scale and crystal phase (that is recoverable from the bulk solution) are phenomenologically interdependent which has yet to be clearly demonstrated.

One of the critical challenges in improving understanding of membrane scaling and membrane crystallisation is the accurate determination of induction time, as this can relate supersaturation to the kinetics of nucleation and crystal growth [17]. [18] describes how the maximum supersaturation that can be achieved at induction ($\Delta C_{max,fm}$) is dependent upon the supersaturation rate. This supersaturation limit is termed the metastable zone width (MSZW) (Fig. 1) [19,20].

Crystallisation at the outer region of the metastable zone is best avoided, as this can introduce high nucleation rates, generating a fine crystal product that is difficult to separate and is of limited value for downstream application [7,21]. In MCr, the supersaturation rate is modified by the membrane flux. Jiang et al. [8] showed how supersaturation rate could be adjusted by changing the feed temperature and the temperature difference between feed and permeate. High feed temperature and temperature difference reduce the critical free energy barrier for nucleation and should favour homogeneous nucleation [11,20]. According to classical nucleation theory, if scaling is to be minimised, supersaturation conditions approaching the solubility limit should also be avoided as it is within this lower region of the metastable zone that the critical free energy barrier for nucleation approaches a maximum (leading to long induction times). Consequently, it is within this region that the membrane is most likely to adjust interfacial energy sufficiently to initiate heterogeneous nucleation (or scaling) [17,22,23]. Therefore, to achieve a crystalline product specification based on size, size distribution and purity, while avoiding scaling, supersaturation should be regulated to a setpoint somewhere between the solubility limit and the outer limit of the metastable zone, which requires modulation of the supersaturation rate.

While homogeneous primary nucleation should be favoured by elevated supersaturation due to the reduction in critical free energy for nucleation (which reduces dependency on the membrane to lower the interfacial free energy requirement), various authors have shown that high feed temperatures enhanced membrane scaling (heterogeneous primary nucleation mechanism) [15,24]. This contradiction may arise from the adoption of high water vapour fluxes which increase interfacial concentration within the boundary layer through simultaneously modifying flux, solute concentration and temperature polarisation. Consequently, there is a higher probability for nucleation to preferentially occur within the interfacial region, that may proceed through an adhesive growth mechanism (often described as heterogeneous nucleation) or through the deposition of crystals that have undergone nucleation in the bulk solution (homogeneous nucleation) [11,25]. To date, the supersaturation rate in MCr, which determines where within the metastable zone that nucleation will commence, has almost exclusively been studied through changes to feed temperature and temperature difference which modify membrane flux [15,24,26]. According to Nývlt [27], the supersaturation rate is independent of membrane flux and is instead dependent on the supersaturation rate of the crystallising solution [8,27,28]. The rate of supersaturation (R) can therefore be modified without changes to feed temperature or temperature difference by an increase in membrane surface area. This permits transition across the MSZW, without modifying conditions within the boundary layer to yield a broader set of kinetic trajectories for nucleation and crystal growth, that may also reduce the probability for scaling when approaching the upper region of the metastable zone where homogeneous primary nucleation is more likely to occur [7].

In this study, we therefore propose to modify supersaturation rate using membrane area to enable the regulation of supersaturation across the MSZW. Through adjusting supersaturation independent of temperature or temperature difference, we will examine the potential to decouple surface scaling from bulk nucleation. This will be complemented by the use of in-line dual optic fibre turbidimetry, for the accurate determination of induction time, which can be used to describe the nucleation kinetics within MCr. As this technique provides direct detection of the first crystals formed in the system, it is also possible to differentiate between the effects of adhesive scaling from those of deposition. Consequently, the mechanisms of scaling and crystallisation can be explored, and the modulation of crystallisation examined across the metastable zone to better inform on strategies to diminish scaling and favour homogeneous (or bulk) nucleation to advance control over crystal growth. Specific objectives are to: (i) characterise the MSZW through adjusting supersaturation rate by membrane area; (ii) relate supersaturation and induction time to MCr using classical nucleation theory; (iii) inform on the relative importance of heterogeneous and homogeneous nucleation during the transition across the metastable zone; and (iv) describe how regulating supersaturation rate within the metastable zone can modify properties of the crystal product.

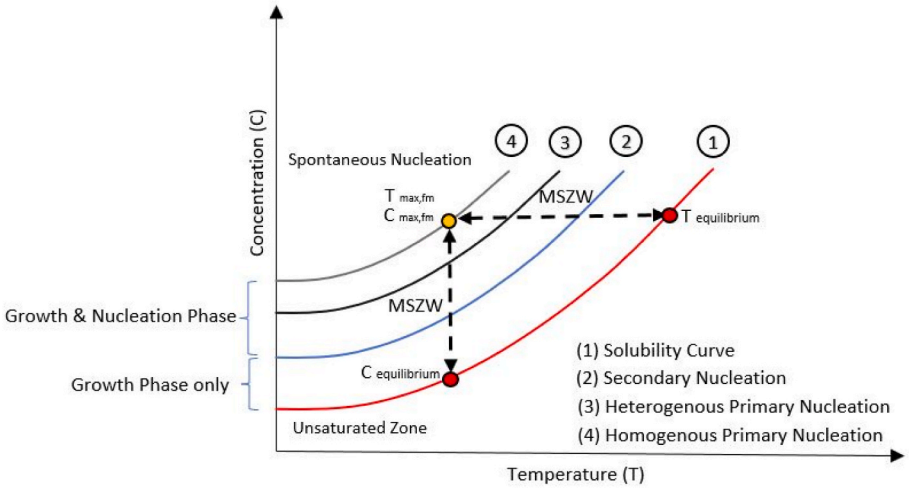


Fig. 1. MSZW as function of temperature and concentration.

2. Materials and methods

2.1. Laboratory set-up for membrane distillation crystallisation experiments

Commercial polypropylene hollow fibres (Accural PP 300/1200, from 3 M Company, Germany) were potted into end plates using epoxy (Araldite). The membrane comprised a pore size of 0.45 μm, wall thickness of 300 μm and porosity of 73% (Table 1). Distribution of the fibres was controlled by spatial arrangement of predrilled holes in the end plates, which ensured a consistent separation distance between fibres for each module studied. Once the hollow fibres were sealed into the end plates, the membrane was mounted into an acrylic membrane module with a 15 mm internal diameter and 150 mm effective length. Membrane modules comprised of 1, 3, 7, 19, 25, and 37 hollow fibres.

Membrane distillation was operated in direct contact mode. The feed was recirculated in the shell-side, and the cold solution recirculated in the lumen-side of the hollow fibre membrane (Fig. 2). Feed concentration was fixed at 23.9 wt% sodium chloride (NaCl) for each condition studied. This concentration is sufficiently below the supersaturation threshold to ensure the experiments reach steady-state prior to achieving a supersaturation of 1, as this ensures the precise discrimination of induction time. The feed solution was heated to 55 ± 1 °C using a heater and heat exchange assembly (Tornado TM IS6, HUBER Ministat230; Radleys, Saffron Walden, UK). Deionised water was used within the cold-side, and was cooled with a chiller (LT ECOCOOL 150, Grant Instruments, Shepreth, UK). The feed and permeate were recycled by a peristaltic pump (Masterflex L/S Digital Pump System, Cole Parmer, St. Neots, UK) to fix velocity at 0.06 m s^{-1}. Increasing fibre number reduced shell-side priming volume, and so the flow rate was adjusted to maintain a velocity of 0.06 m s^{-1}. By maintaining a comparable liquid velocity (and adjusting the heat input), a comparable temperature difference (ΔT) of 20 ± 2 °C was set for each module tested. The only exception was the 1 hollow-fibre module, which necessitated a feed velocity of ~0.6 m s^{-1} to maintain the same ΔT. While a constant liquid velocity was maintained for each module, the Reynold's number declined with an increase in hollow fibre number due to the reduction in cross sectional area. However, laminar flow conditions were consistently established within each membrane module tested (*Re* 134 to 1370, for 37 and 1 HF respectively). Temperature and conductivity were measured in-line (El1034 Temperature Prop, LabJack Corporation, Lakewood, USA). An in-line turbidity sensor was used to detect the onset of nucleation. The dual optic fibre construction delivers high resolution for low turbidity measurements through detection of backscatter and is used extensively in industry for the determination of induction (InPro8200/S/Epoxy/120, Mettler Toledo, Manchester, UK). Experiments were conducted in triplicate, and the average reported.

2.2. Characteristics of produced crystals and membrane surface scaling

Crystals collected from the bulk were filtered through a 0.45 μm nylon filter (Whatman, Dorset, UK) and dried over a desiccant for 48 h (temperature ~23 °C) before weighing and sizing. Optical microscopy was used to collect images (Lumenera Infinity 3-3 Camera with 5/0.12 160/- lens) which were analysed for the determination of crystal size using proprietary software (Image ProPremir 9.2). Crystal size distributions were determined in triplicate for each sample, with each distribution constructed from a minimum of 1300 crystals per batch as this exceeded the threshold at which the standard error of the distribution achieved a minimum. The coefficient of variation (CV) was calculated according to the following equation [29]:

$$CV = \frac{L_{84\%} - L_{16\%}}{2\,L_{50\%}} \tag{1}$$

where L (μm) is the crystal length of the cumulative percent function at indicated percentage. A high precision balance (range 0.02 to 62g, error ±0.0001g, Fisherbrand™, Loughborough, UK) was used to weigh each of the scaled membranes after operation, and the crystal mass normalised by membrane surface area (g m^{-2}). Scanning electron microscopy (SEM) was used to explore surface scaling characteristics using an acceleration voltage of 20 kV (TESCAN VEGA3, Cambridge, UK).

2.3. Mass and heat transfer characterisation in membrane distillation

Permeate flux *N* (kg m^{-1} h^{-1}) was calculated experimentally as [30]:

$$N = \frac{m}{A \times \Delta T} \tag{2}$$

where m is the mass of permeate (kg), A is the effective membrane area (m^2), and ΔT is the time interval (h). Heat transfer comprises of the latent heat Q_v (W m^{-2}) demand for water vapour transport, and heat conduction through the membrane Q_c (W m^{-2}) [30]:

$$Q = Q_c + Q_v = \left(\frac{k_m}{\delta_m}\right)\left(T_{fm} - T_{pm}\right) + NH_{V,T} \tag{3}$$

where δ_m (m) is the membrane thickness, and k_m (W m^{-1} K^{-1}) is the membrane thermal conductivity [31]:

$$k_m = k_p(1-\varepsilon) + k_g\varepsilon \tag{4}$$

where k_p (W m^{-1} K^{-1}) is the polymer thermal conductivity and k_g (W m^{-1} K^{-1}) is the air thermal conductivity. $H_{V,T}$ (KJ kg^{-1}) is the vapour latent heat [14,32]:

$$H_{V,T} = 1.7535\ \mathrm{T} + 2024.3 \tag{5}$$

where $\mathrm{T} = \frac{T_{fm}+T_{pm}}{2}$, is the average temperature at the membrane surface.

Table 1
Membrane and module specification.

Property	Units	Value	Fibre no.					
			1	3	7	19	25	37
Internal diameter	(di, m)	0.0012						
Outer diameter	(do, m)	0.0018						
Wall thickness	(m)	0.0003						
d_i/d_o	-	0.67						
Pore size	(μm)	0.45						
Porosity	(%)	73 ± 2						
Contact angle[a]	(°)	131						
Fibre length	(m)	0.15						
Shell inner diameter	(m)	0.015						
Packing density	(%)		1.5	4.4	10.2	27.7	36.4	53.9
Membrane area	(cm^2)		8.5	25.5	59.4	161.2	212.1	313.9

[a] Measured using water (Davey et al., 2020).

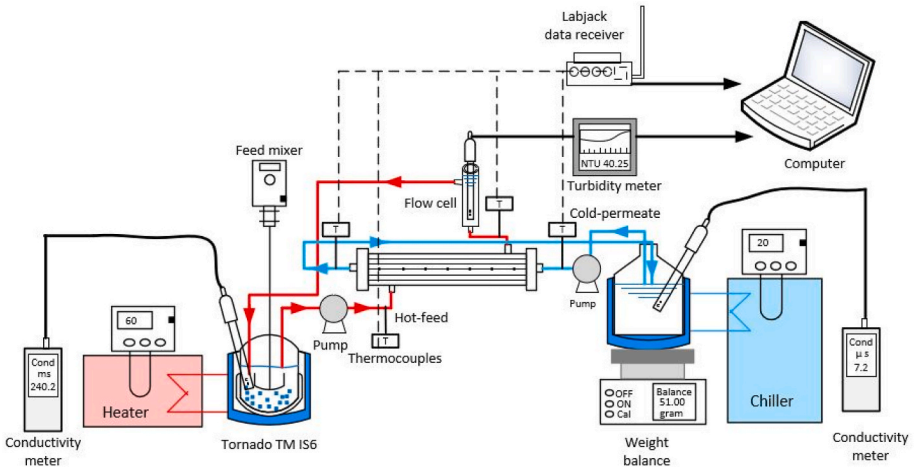


Fig. 2. Schematic diagram of the Membrane Distillation Crystallisation setup.

The feed and permeate temperature adjacent to membrane surface, T_{fm} and T_{pm} (K), can be calculated by iteration [26] from the heat transfer relationship [30]:

$$T_{fm} = T_f - \left(T_f - T_p\right)\left[\frac{1/h_f \times d_i/d_o}{1/h_f \times d_i/d_o + 1/(h_m + h_v) + 1/h_p}\right] \quad (6)$$

$$T_{pm} = T_p - \left(T_f - T_p\right)\left[\frac{1/h_p}{1/h_f \times d_i/d_o + 1/(h_m + h_v) + 1/h_p}\right] \quad (7)$$

where d_i/d_o (unitless) is the ratio of inner/outer diameter, T_f and T_p (K) are the bulk temperature in feed and permeate, $h_m = k_m/\delta_m$ (W m^{-2} K^{-1}) is the heat transfer coefficient of the membrane, and h_v (W m^{-2} K^{-1}) is the heat transfer coefficient involved with vapour flow, assuming constant membrane temperature:

$$h_v = \frac{NH_{v,\left(T_{fm}+T_{pm}\right)/2}}{\left(T_{fm} - T_{pm}\right)} \quad (8)$$

where h_f and h_p (W m^{-2} K^{-1}) are the heat transfer coefficients associated with the liquid film of feed and permeate sides and can be calculated from the following equation:

$$h_{f,p} = Nu \times \frac{k_{f,p}}{d_{h_{f,p}}} \quad (9)$$

where $k_{f,p}$ (W m^{-1} K^{-1}) is the thermal conductivity of feed/permeate, $d_{h,f,p}$ (m) is the hydraulic diameter of feed/permeate flow channel, *Nu* is Nusselt's number, Re is Reynold's number and Pr is Prandtl's number (Appendix).Thus, the temperature difference between the bulk solution and membrane surface can be described by the temperature polarisation coefficient:

$$TPC = \frac{T_{fm} - T_{pm}}{T_f - T_p} \quad (10)$$

The interfacial concentration C_{fm} (g $_{NaCl}$ g^{-1} $_{solution}$) close to the membrane surface is distinct from the feed bulk concentration C_{fb} (g $_{NaCl}$ g^{-1} $_{solution}$) and can be described by the concentration polarisation [33]:

$$CPC = \frac{c_{fm}}{c_{fb}} = exp\left(\frac{N}{\rho \times k_s}\right) \quad (11)$$

where N (kg m^{-1} h^{-1}) is the permeate flux, ρ (kg m^{-3}) density of the solution and k_s (m s^{-1}) is the solute mass transfer coefficient which can be estimated based on (Appendix; [34].

2.4. Nucleation kinetics characterisation

The nucleation rate J (No. m^{-3} s^{-1}) is expressed according to Arrhenius's approach as follows, where ΔG* is the critical nucleation barrier at a given supersaturation [35]:

$$J = A\exp\left(-\frac{\Delta G*}{K\,T}\right) = A\exp\left(-\frac{16\pi v_*^2\gamma^3}{3(k_BT)^3\,ln^2\,s}\right) \quad (12)$$

$$\Delta G* = \frac{16\pi v_*^2\gamma^3}{3(k_BT)^2\,ln^2\,s} \quad (13)$$

where ΔG* (kJ mol^{-1})is the critical nucleation barrier at a given supersaturation, k_B (1.38 x 10^{-23} J K^{-1}) is the Boltzmann constant [36], $v_o = M/\rho_{cry}N_a$ (m^3) is the molecular volume, M (kg mol^{-1}) is the molar weight, ρ_{cry} is crystal density, N_a is Avogadro's number (6.022 x 10^{23} molecules mol^{-1}), T is the nucleation temperature (K), S=C/C* (unitless) supersaturation degree, γ is the interfacial energy (mJ m^{-2}). Nucleation rate and induction time have an inverse relationship according to classical nucleation theory [21]:

$$t_{ind} \propto \frac{1}{J} \quad (14)$$

which can be related to the extent of supersaturation:

$$\ln t_{ind} = \ln A + \left(\frac{16\pi v_*^2\gamma^3}{3(k_BT)^2\,ln^2\,s}\right) = \ln A + \left(\frac{B}{ln^2\,s}\right) \quad (15)$$

where A (m^{-3} s^{-1}) is the pre-exponential parameter (intercept), B is the thermodynamic parameter for nucleation (gradient) [37]. The linear relationship between ln(t_{ind}) and 1/(ln^{2}S), enabling determination of nucleation mechanism (homogenous or heterogenous) from the degree of linear slopes.

The MSZW was calculated by adoption the approach proposed by Ref. [27]; where the maximum MSZW at membrane surface $\Delta C_{max.fm}$ (mg g^{-1} solution) is assumed to be proportional to the concentrating rate within MCr (R' = dc/dt) (g 100g solution^{-1} h^{-1}) [8,18,38] as follows:

$$\Delta C = \left(\frac{dC}{dT}\right)_T R' \quad (16)$$

$$R' = \left(\frac{dCo}{dt}\right)_t = \frac{F_p C_0}{m_0 - \int_0^t F_P d\tau} \quad (17)$$

where F_p (kg h^{-1}) is the permeate flow rate. Following the approach of [27]; the relation between the nucleation rate J (No. m^{-3} s^{-1}) and the

maximum supersaturation $\Delta C_{max.fm}$ (g_{NaCl} g^{-1} $_{solution}$) adjacent to membrane surface can be expressed by the empirical power-law equation:

$$J = k\left(\Delta C_{max,fm}\right)^{n} \tag{18}$$

where k (No. m^{-3-n} s^{-1+n}) is the nucleation rate constant, n (unitless) is the nucleation order, $\Delta C_{max,fm}$ is the maximum supersaturation (c_{fm}-c^*), c_{fm} (g_{NaCl} g^{-1} $_{solution}$) is the feed membrane surface concentration and c^* (g_{NaCl} g^{-1} $_{solution}$) is the saturation concentration. Combining equations (21) and (22), the nucleation rate (J) provided by continuous solvent removal is:

$$J = k\left(\Delta C_{max,fm}\right)^{n} = \left(\frac{dc_0}{dt}\right)_t = \frac{F_p C_0}{m_0 - \int_0^t F_P d\tau} \tag{19}$$

Once supersaturation reaches the MSZW limit ($\Delta C_{max,fm}$), the logarithm form is described as:

$$\ln\left(\Delta C_{max,fm}\right) = \frac{1}{n}\ln\left(\frac{C_0}{k}\right) + \frac{1}{n}\ln\left(\frac{F_p}{m_0 - \int_0^t F_P d\tau}\right) \tag{20}$$

From linearly fitting $\ln(\Delta C_{max,fm})$ and ln(R'), the nucleation rate constant (k) and nucleation order (n) can be calculated.

3. Result and discussion

3.1. Impact of increasing membrane area on nucleation at fixed flux

To examine the effect of increasing membrane area on induction (the onset of nucleation), permeation flux was measured as this is generally considered to provide the driving force for nucleation (Fig. 3) [9]. A constant temperature difference (ΔT) of 20 ± 2 °C was maintained by fixing feed velocity for each membrane module. Consequently, comparable membrane flux of around 3.5 kg m^{-2} h^{-1} was achieved for each membrane, except for the 37 HF module which recorded a slightly lower flux of 2.8 kg m^{-2} h^{-1}. This slight reduction in flux may have been induced by the higher packing density (Table 1) which has been shown to impose preferential flow patterns that can reduce the perceived local superficial velocity [39]. Importantly, while comparable fluxes were achieved for each membrane, the extent of supersaturation that was achieved before flux decline, was dependent upon the membrane surface area (Fig. 3b).

To illustrate, a significant flux decline was observed at 895, 57 and 47 min for 1, 25 and 37 HF membrane modules respectively. Each flux profile comprised of three consecutive stages (Fig. 3b, inset): (i) a period of steady-state filtration, with a slow progressive decline in flux initiated by the increase in solute concentration which reduced water activity

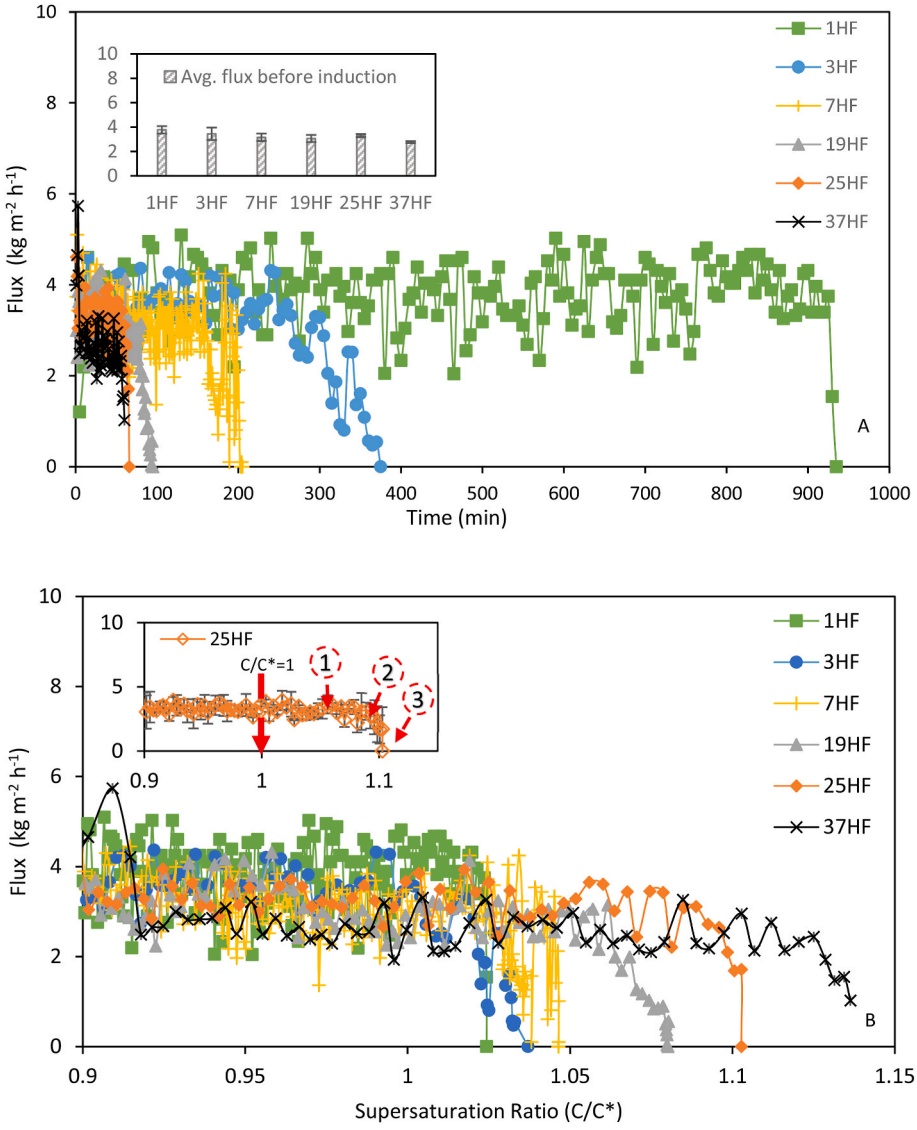


Fig. 3. Permeation flux during MCr operation time for different membrane modules: (A) over time; and (B) evidencing flux decline against the progressively supersaturated fluid. Boundary conditions: T_{bulk}, 55 ± 1 °C; $\Delta T_{membrane}$, 20 ± 2 °C; initial feed NaCl concentration, 23.9 wt%. Standard error of permeation flux was calculated based on differences in triplicate measurements for each membrane modules; 1 HF, 3.8 ± 0.3; 3HF, 3.4 ± 0.5; 7HF, 3.2 ± 0.3; 19HF, 3.1 ± 0.3; 25HF, 3.3 ± 0.1; 37HF, 2.8 ± 0.1.

[40,41]; (ii) an inflection point, which marks a disruption in water vapour transport; and (iii) a rapid loss in water vapour flux [26,30]. This inflection point is often associated to the initiation of nucleation, while the subsequent reduction in vapour pressure is attributed to the mass and heat transfer resistance provided by the crystal phase which can develop at the membrane surface through adhesive growth or via deposition following nucleation and crystal growth in the bulk solution [9,17,26].

Turbidimetric profiles confirmed the onset of bulk nucleation (Fig. 4). The time required to produce a crystal phase decreased from 930 min for 1 fibre, to 60 min for the 37 HF membrane. Bulk nucleation was consistently observed after the rapid flux decline was observed, while the time between the flux decline and bulk nucleation shortened as membrane area was increased. The time between the saturation state (c/c*, 1) and the first detected nuclei is defined as the induction time, which indicates the onset of primary nucleation (J.W [22,37,42]. (Fig. 4B). The induction time is therefore a measure of the kinetic metastability of solution. With an increase in membrane area, induction time decreased, but the supersaturation level achieved at induction increased. For instance, with 1 HF module, induction time was 143 min, corresponding to bulk supersaturation (c/c*) of 1.02, whereas an induction time of 24 min, and c/c* of 1.12 was recorded for the 37 HF module. This inverse relationship between induction time and supersaturation is in accordance with the literature [21,22], when the crystallising solution is exposed to an increase in solvent removal rate. In this study, the increase in solvent removal rate is enabled through the increase in membrane area (despite constant flux, temperature and ΔT), and it is through these higher solvent removal rates that elevated supersaturation levels can be reached within the crystallising solution. This is evidenced by constructing the corresponding MSZW, which describes the difference between the solubility limit and the maximum supersaturation limit at which nucleation occurs [43] (Fig. 5).

Increasing membrane area from 1 to 37 HF resulted in an increase in MSZW from 27.6 to 30.1% wt./wt. According to Ref. [27]; higher supersaturation rates reduce the critical free energy barrier for nucleation due to the higher driving force provided by the elevated supersaturation gradient [8,38,44]. Consequently, membrane area can be adjusted to mediate the size of the MSZW, which will likely inform the kinetics of nucleation and crystal growth, in addition to the specific primary nucleation mechanism which determines the probability for scaling phenomena that remain an acknowledged limitation for membrane distillation and crystallisation [8,45].

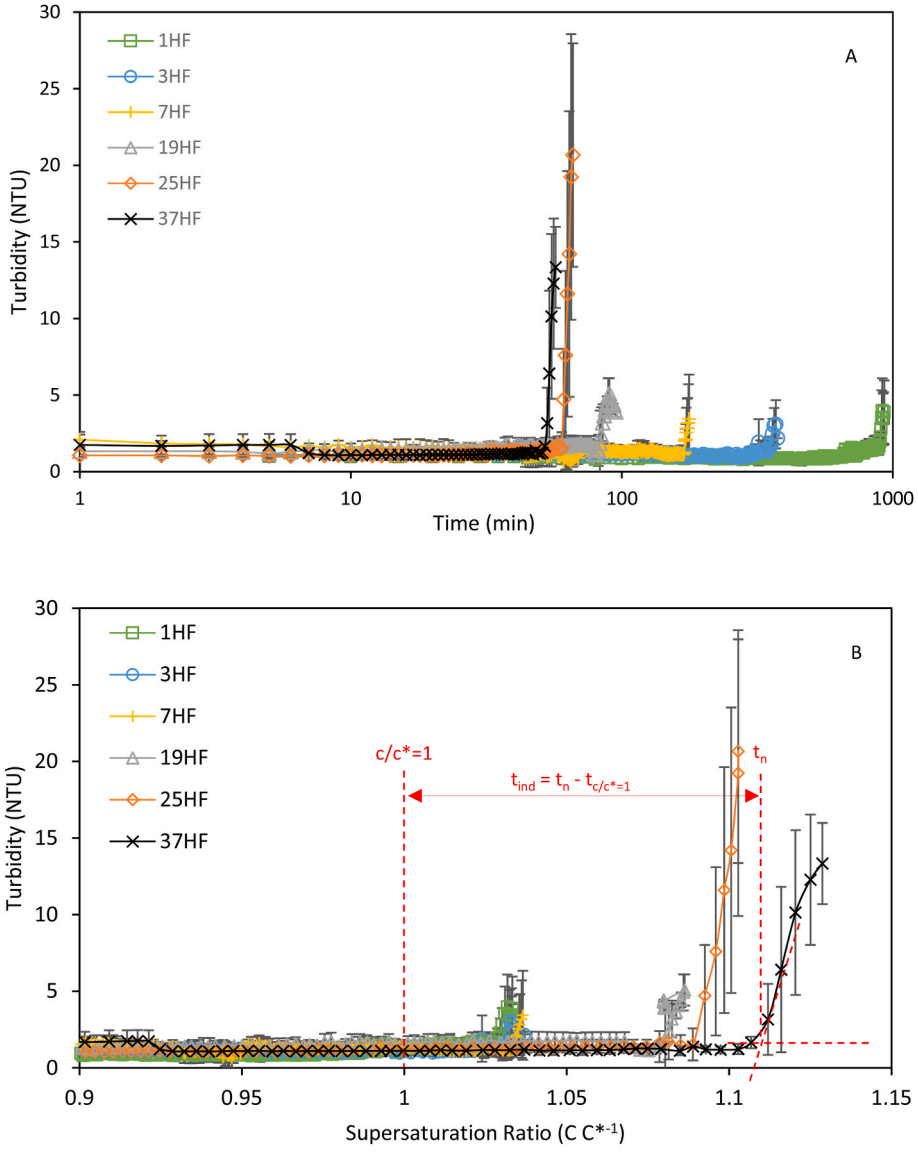


Fig. 4. Turbidity profile during MCr operation for membranes comprised of increasing surface area: (A) based on operating time; (B) based on bulk supersaturation. Boundary conditions: T_{bulk}, 55 ± 1 °C; $\Delta T_{membrane}$, 20 ± 2 °C; initial feed NaCl concentration, 23.9 wt%.

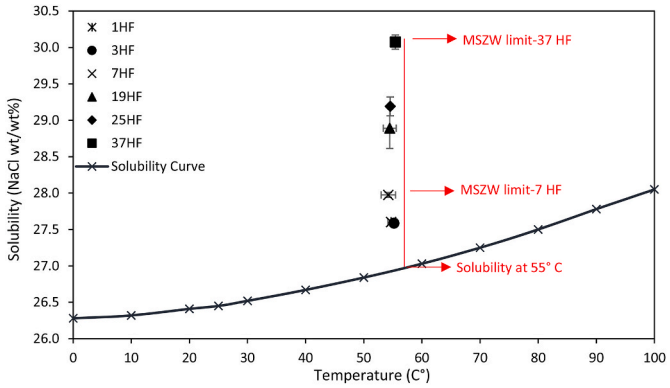


Fig. 5. A broad metastable region is created by increasing membrane area at fixed flux. Boundary conditions: T_{bulk}, 55 ± 1 °C; $\Delta T_{membrane}$, 20 ± 2 °C; initial feed NaCl concentration, 23.9 wt%.

3.2. Shifting induction time by using membrane area to increase concentration rate

Since mass and heat transfer can collectively modify supersaturation locally, concentration and temperature polarisation were characterised to confirm that increasing membrane area did not significantly adjust the boundary layer conditions which can otherwise increase the maximum supersaturation near the membrane interface at induction ($\Delta C_{max,fm}$) (Fig. 6).

The temperature polarisation coefficient (TPC) was reasonably consistent when increasing membrane area. Higher surface area will increase conductive heat transfer losses, while the greater convective losses can be expected from the increase in net water vapour transport [40,46,47]. However, as an equivalent fluid velocity was sustained for each module, the losses are in proportion to surface area and an equivalent TPC profile was developed, which was confirmed by the consisent ΔT of 20 ± 2 °C achieved for each module. Since the solubility-temperature dependency of NaCl is relatively flat [26], the solubility constant for NaCl within the boundary layer is not markedly affected by the increase in membrane area. A slight reduction in concentration polarisation coefficient (CPC) from 1.06 to 1.03 was observed when the supersaturation rate was increased from -1.01 g 100 g^{-1} h^{-1} for 1 HF to 3.24 g 100 g^{-1} h^{-1} for 37 HF. Since similar hydrodynamics were consistently employed, this slight modification of CPC may relate to the extent of supersaturation achieved within the bulk solution with an increase in supersaturation rate, which will also reduce the relative vapour pressure at induction.

According to Ref. [18]; the maximum supersaturation at induction is proportional to the supersaturation rate and is linearly dependent on where within the metastable zone that nucleation occurred. This was confirmed by constructing the correlation between supersaturation rate (LnR′) and the corresponding metastable zone width ($\Delta C_{max,fm}$) (Fig. 7A). The lowest $\Delta C_{max,fm}$ of 2.62 mg_{solute} $g^{-1}_{solution}$ was recorded for 1HF corresponding to LnR' -1.01 g 100 g^{-1} h^{-1}, whereas a $\Delta C_{max,fm}$ of 3.73 mg g^{-1} was recorded for the 37HF module as LnR' increased to 3.24g 100 g^{-1} h^{-1}. The supersaturation rate is a direct analogy to nucleation rate [18]. Acordingly, the nucleation kinetics were ascertained from line fitting to provide a nucleation order n = 0.23 (−) and nucleation constant k = 2.91 No. m^{-3-n} s^{-1+n}. Nucleation order and constant are physical parameters that describe nucleation rate, relating the MSZW dependency to the concentrating rate in which its value defines the growth of stable nuclei to visible entities [28,48]. Widening of the MSZW by the supersaturation rate is consistent with the literature [20]. An increase in supersaturation rate reduces the time required to achieve induction (Fig. 7B). This is because the elevated supersaturation lowers the energy barrier for nucleation by providing a greater driving force for solute transformation to a solid-phase [49]. Induction time is therefore inversely related to nucleation rate through classical nucleation theory, where higher nucleation rates are achieved at the shortest induction time [50].

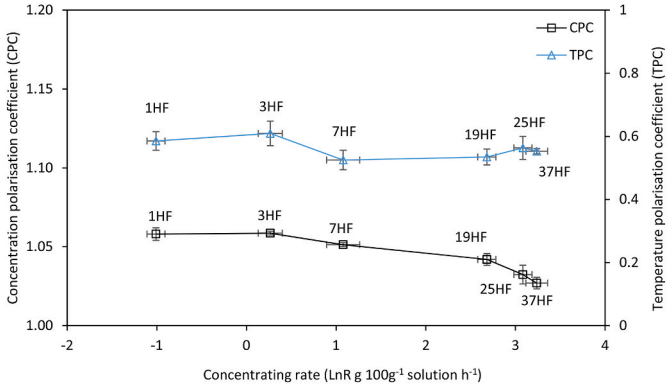


Fig. 6. The CPC and TPC of supersaturation at induction over different concentration rate (ln R′). bulk (°C) = (55 ± 1), ΔT membrane (°C) = (20 ± 2), Velocity of feed and permeate = 0.06 m s^{-1}, initial feed concentration NaCl (wt. %) = 23.9.

By increasing membrane area from 1 to 37HF, induction time reduced by 119 min, indicating a significant increase in nucleation rate from 8.9 x 10^{-7} to 2.2 x 10^{-5} No. m^{-3} s^{-1} (based on CNT) without obviously modifing polarisation within the boundary layer. The Gibbs free energy barrier is substantially reduced by the increase in $\Delta C_{max,fm}$ at induction. In such conditions, primary nucleation is less dependent on modification of the interfacial energy, and therefore the probability for nucleation to proceed through a homogeneous mechanism is increased [9,22,51]. This is contradictory to suggestions within the existing MCr literature, which hypothesise that it is the supersaturated conditions within the boundary layer complemented by reduction in interfacial energy introduced by the membrane that overcome the free energy barrier for nucleation [11,26]. In this study, we propose that the high supersaturation driving force imposed by the increase in supersaturation rate subsequently imposes kinetically controlled crystallisation with nucleation being more dependent on development of the closest metastable form and less dependent on the heterogeneous substrate [20]. This is supported by comparison of supersaturation within the bulk and interfacial boundary layer adjacent to the membrane at induction (Fig. 8). As the supersaturation rate is modified by membrane area rather than boundary layer characteristics (which would not be the case for temperature or ΔT), the difference in supersaturation between the bulk solution and interfacial region becomes negligible as supersaturation rate is increased. Consequently, it can be inferred that the probability for nucleation occurring within the bulk solution rather than at the membrane surface is comparable or greater within the upper region of the metastable zone.

3.3. Supersaturation rate defines the primary nucleation mechanism

To distinguish which primary nucleation mechanism was dominant when supersaturation rate was controlled by membrane area, rather than by local mass and heat transfer mechanisms (as with feed temperature and ΔT), diagnostic examination of scaling was conducted on each HF module following induction (Fig. 9). An increase in the supersaturation rate reduced crystal mass deposition. Membrane scaling is thought to proceed via two distinct mechanisms: (i) adhesive growth, following nucleation within the vicinity of the membrane; and/or (ii) the deposition of crystals that have undergone primary homogeneous nucleation in the bulk solution [17,24,51]. Microscopic examination of each membrane surface illustrated distinct growth characteristics (Fig. 10).

Deposition on the hollow-fibre membranes that fostered low supersaturation rates (below 7HF), exhibited significant surface coverage,

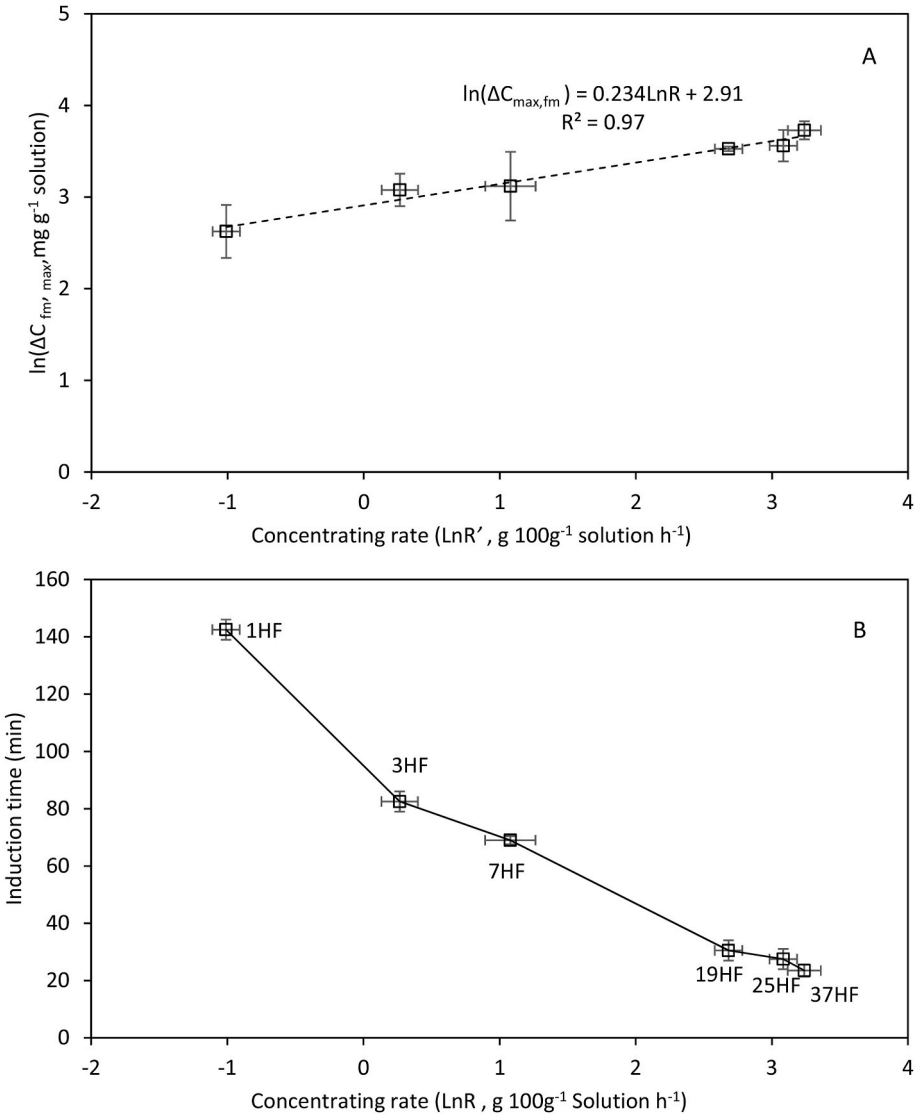


Fig. 7. (A) The dependence of Δcfm, max on concentrating rate (ln R′) according to equation (20) for different membrane modules, (B) The dependence of induction time on concentrating rate (ln R′) for different membrane modules, bulk (°C) = (55 ± 1), ΔT membrane (°C) = (20 ± 2), velocity of feed and permeate = 0.06 m s^{-1}, initial feed concentration NaCl (wt. %) = 23.9.

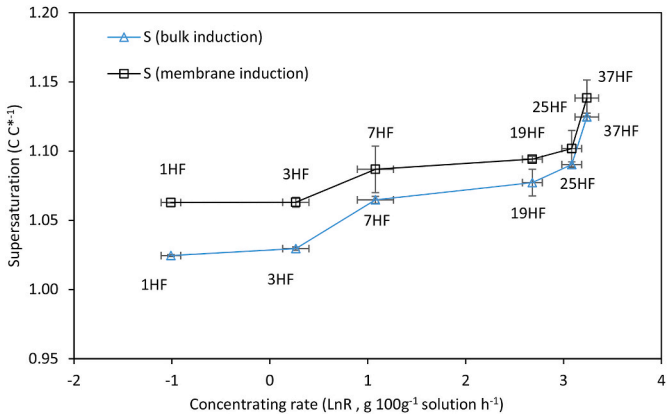


Fig. 8. Supersaturation degree of bulk and membrane over different concentration rate (ln R′), bulk (°C) = (55 ± 1), ΔT membrane (°C) = (20 ± 2), velocity of feed and permeate = 0.06 m s^{-1}, initial feed concentration NaCl (wt. %) = 23.9.

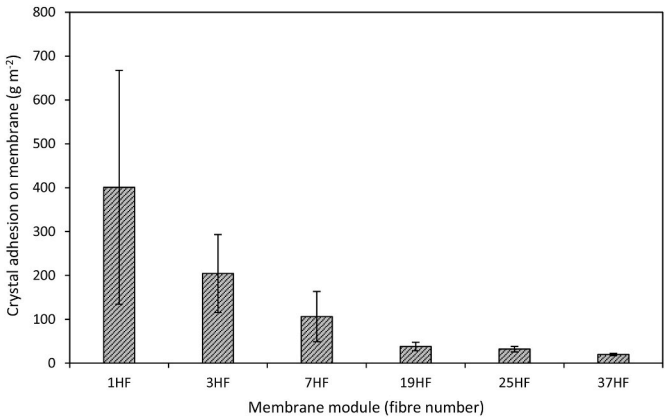


Fig. 9. Membrane crystal adhesion for modules of different surface area, which indicates the reduction in surface nucleation with an increase in concentration rate.

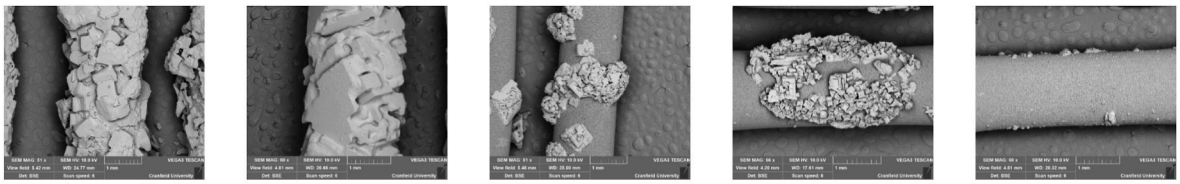


Fig. 10. Scanning electron microscope (SEM) images highlighting reduced surface adhesion (scaling) as concentration rate increases through an increase in membrane area. Scale bar: 1 mm.

while the cubic morphology synonymous with NaCl was difficult to clearly observe. For hollow-fibre membranes that promoted higher supersaturation rates (>19HF), less deposition was noted and was confined to discrete areas, that were fewer in number as membrane surface area increased. Crystalline morphology appeared distinct from that observed at low supersaturation rates, with cubic orientation more evident but with evidence of interconnected dendritic outgrowths. This is characteristic of highly supersaturated conditions which migrate from diffusion limited to surface-integration limited crystal growth, where surface area is rapidly formed by secondary nucleation mechanisms [52].

The kinetic transition across the metastable zone was subsequently characterised to relate the specific primary nucleation mechanism to the extent and character of the deposition observed. While induction time and the supersaturation level at induction are recognised as critical crystallisation parameters that underpin scale formation, such data is rarely reported in the membrane literature [17]. In-line turbidimetry enabled direct measurement of induction time and evidenced two discrete regions of supersaturation with very different gradients (Fig. 11).

Induction time is a kinetic parameter that is characterised by two distinct supersaturation regions within the metastable zone, where the shallow gradient formed at low supersaturation is indicative of heterogeneous primary nucleation while the steeper curve formed at higher supersaturation represents a homogeneous primary nucleation mechanism [20,22]. The gradient of the curves represents the interfacial energy required to create a thermodynamically stable nucleus within those discrete regions of supersaturation (Datta & Grant, 2005). In this study, the region of heterogeneous primary nucleation corresponded to modules with 1–7 HF where low supersaturation rates were observed, and substantive scaling was detected (Fig. 10). The gradient of the curve representing the homogeneous primary nucleation mechanism, was seven times higher, indicating the energy barrier for nucleation to be considerably lower when higher supersaturation rates were employed (>19 HF) and corresponded to supersaturation levels measured at

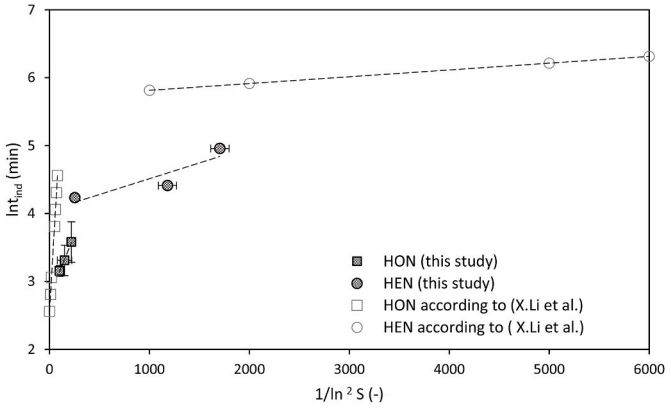


Fig. 11. ln (tind) versus 1/ln2S for different membrane modules show different nucleation mechanism. The change in slope indicates different nucleation mechanism as reported in Li et al. (2009).

induction (C/C*) of 1.075-1.117 (Table 2). This transition between nucleation mechanisms when moving across the metastable zone is comparable to previous literature observations (Fig. 11, Table 2) [20,22,53]. The limited supersaturation observed for 1 to 7 HF restricts the driving force for nucleation, which increases the dependency on heterogeneous sites to modify the interfacial free energy sufficient to overcome the critical free energy barrier for nucleation [17,22,54]. For highly soluble compounds such as NaCl, nucleation tends to be more critically dependent on a heterogeneous catalyst due to the low supersaturation achieved [11].

Low supersaturation tends to favour crystal growth which may explain the substantive scaling observed [55–57]. This hypothesis is supported by the limited crystal yield observed for supersaturation rates characterised as primarily undergoing a heterogeneous primary nucleation mechanism (Fig. 12). As the supersaturation rate was increased, the crystal phase produced in the bulk solution improved, and was complemented by a reduced scaling rate (Fig. 13), which is analogous to the description of a homogeneous primary nucleation mechanism [17,20]. Several mechanisms have been proposed to explain how the membrane promotes heterogeneous nucleation that include solute entrapment, enhanced molecular orientation and a reduction in interfacial energy [7]. In this study, microscopic examination evidenced significant scaling within the pores that dissipated with an increase in supersaturation rate. While this observation may be specific to conditions where supersaturation rate is moderated without substantive changes to the boundary layer, it infers that solute entrapment within the pores constitutes a significant role in initiating scaling.

3.4. How supersaturation rate determines crystal growth characteristics

The crystal phase recovered from the bulk solution was examined to understand how crystal size, size distribution and morphology may be influenced by the supersaturation rate. The crystal growth kinetics broadly correlated to where within the metastable zone that growth was initiated, with the crystal size distribution observed to shift right as supersaturation rate was increased (Fig. 14). To illustrate, mean crystal size ($L_{4,3}$) was 195 μm at the highest supersaturation rate (37 HF), and reduced to 107 μm at the lowest supersaturation rate (Table 3). This is not consistent with classical crystallisation where fewer, larger crystals are generally favoured at low supersaturation rates [44]. This may explained by the competition between nucleation and crystal growth in highly supersaturated solutions (particularly relevant for high solubility aqueous salts) characterised by short induction times which tend to favour Ostwald ripening, where the produced nuclei have little time to grow into a thermodynamically stable phase, which results in dissolution and the redeposition onto stable crystals resulting in substantive growth [58]. Higher supersaturation generally constrains crystal growth, as the high nucleation rates inhibit ion availability for growth (Lewis et al., 2015). While a similar response may be expected for MD operation when ΔT is adjusted, as this will raise the supersaturation profile only within the boundary layer, this is not the case when increasing supersaturation with membrane area, as the supersaturation profiles within the bulk and boundary layer both increase. Consequently, despite the higher supersaturation profile instigating higher nucleation rates when membrane area is increased, there is likely to be

Table 2
Results analysis of nucleation parameters based on correlation of ln (tind) versus $1/\ln^2 S$.

T/K	Nucleation	Intercept (K)	Slope (m)	R^2	Supersaturation Range (c c^{*-1})	Recovered mineral	Molecular weight (g mol^{-1})	Solubility	Ref.
328.15	Homogeneous Heterogeneous	2.78 4.05	0.0036 0.0005	0.99 0.81	1.075-1.117 1.025-1.065	NaCl	58.44	370 (g L^{-1})	This Study
323.15	Homogeneous Heterogeneous	6.47 7.88	0.0918 0.0071	0.99 0.94	1.27-1.40 1.10-1.23	Analgin	333.34	0.027 (mol mol^{-1})	[21]
283.15	Homogeneous Heterogeneous	2.56 5.71	0.025 0.0001	1 1	1.60-1.81 1.49-1.51	KCl	74.55	312 (g L^{-1})	(Li et al., 2009)

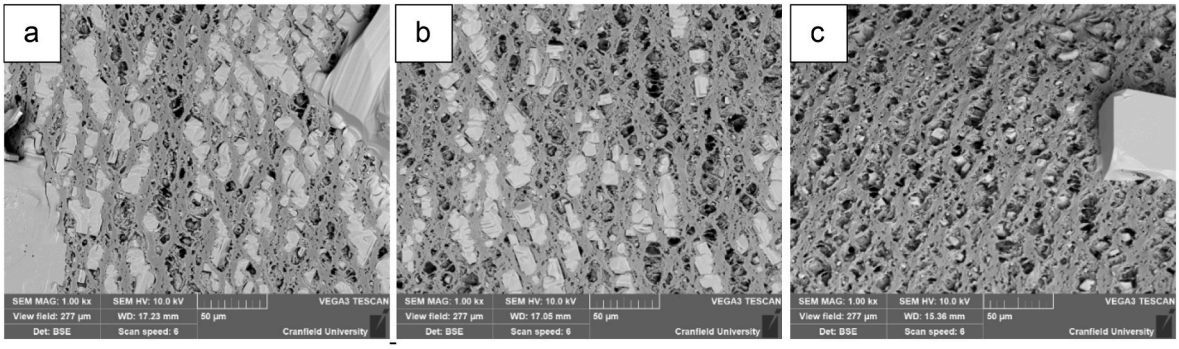


Fig. 12. Scanning electron microscope (SEM) images of membrane pores from membranes used in different sized modules, illustrating how the increase in concentration rate with membrane area reduces nucleation within the pore structure. Scale bar, 50 µm. (a) 7HF; (b) 19HF; (C) 25HF.

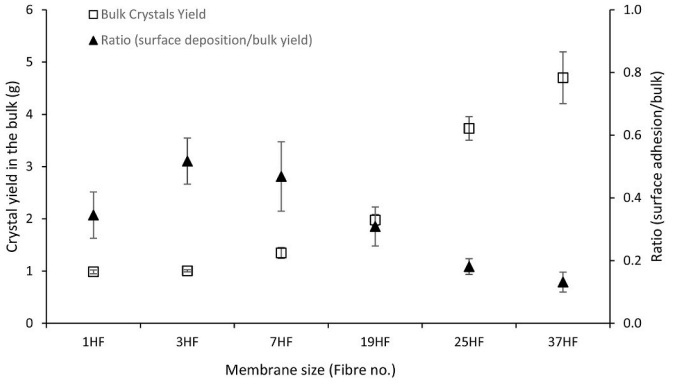


Fig. 13. Crystal yield produced in the bulk solution when using membranes modules of different size to increase concentration rate.

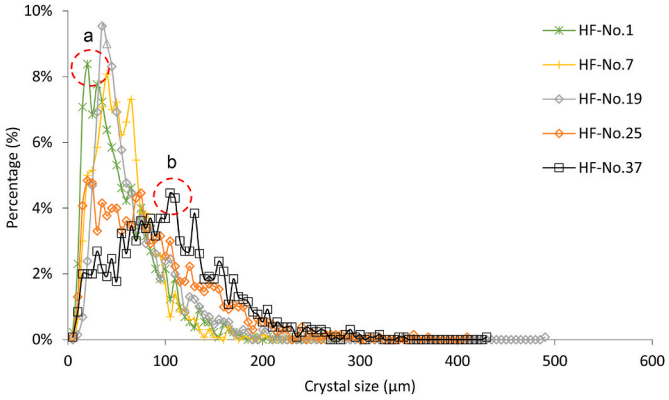


Fig. 14. Crystals Size Distribution (CSD) based on volume fraction (%).

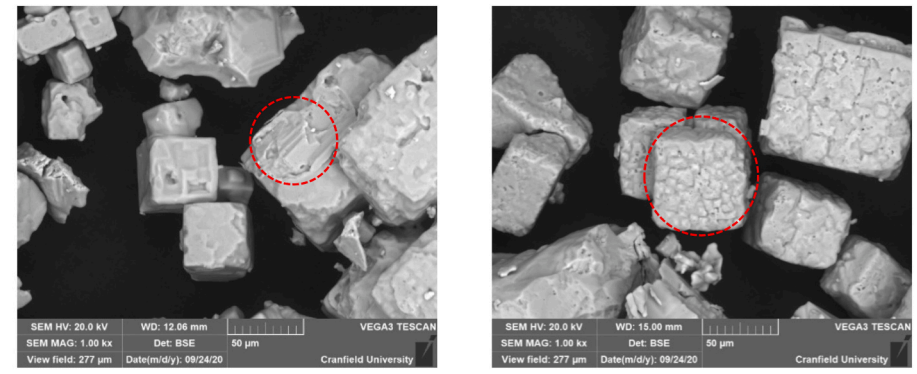
sufficient ion saturation within the bulk condition following nucleation to enhance growth.

The coefficient of variation (CV) represents the distribution of produced crystal sizes which can be important for product end use [29]. In general, the CV was lower for the higher supersaturation rates examined. For each supersaturation rate studied, the crystal phase produced in the bulk solution was of cubic habit which conforms with expected growth patterns [14]. However, modifying the supersaturation rate with membrane area initiated morphological distinctions in the end crystal product (Fig. 15).

The cubic face formed at high supersaturation rates (e.g. 37 HF) was characterised by a 'rough growth' pattern, whereas under low supersaturation rates (e.g. 1 HF) the growth followed a spiral growth mechanism [59]. This can be explained based on the kinetic-based model that describes the absorption and subsequent diffusion of molecules on the

Table 3
CSD parameters of recovered crystals from different membrane sizes.

Membrane module	Volume-based mean crystal size ($L_{4,3}$, µm)	Coefficient of variation (CV, %)	Volume-based crystal's percentile (µm)		
			L_{10}	L_{50}	L_{90}
37 HF	195 ± 1	0.49 ± 0.07	31 ± 8	98 ± 19	178 ± 13
19 HF	184 ± 10	0.56 ± 0.08	27 ± 7	51 ± 4	115 ± 9
7 HF	112 ± 17	0.63 ± 0.12	12 ± 7	30 ± 15	75 ± 5
1 HF	107 ± 23	0.60 ± 0.04	12 ± 2	29 ± 11	66 ± 24



(a) (b)

Fig. 15. Scanning electron microscope (SEM) images of: (a) crystals produced from 1HF experiment (scale bar, 50 μm), (b) crystals produced from 37 HF experiment, evidencing distinct growth patterns upon increasing concentration rate.

crystal surface until incorporated into the crystal lattice [59]. At a higher supersaturation level, the growth unit is incorporated into the crystal lattice with either two or three bonding sides, invoking rough growth pattern [59,60]. While at lower supersaturation the growth unit is incorporated into the crystal lattice at a flat surface with one bonding side, providing a faster growth in the centre compared to edges [59,60]. Consequently, crystal morphology depends on the supersaturation environment that determines the crystal growth mechanism.

4. Conclusions

In this study, the metastable zone has been quantitatively described in membrane distillation crystallisation by using in-line turbidimetry to provide a framework with which to define explicit scaling and crystal growth mechanisms which to date have been rarely described. Supersaturation rate was modified by membrane area rather than through adjustment of water vapour flux. This approach enabled the detailed characterisation of scaling mechanisms that could be explained through classical nucleation theory and may be more difficult to delineate when modifying boundary layer hydrodynamics, feed temperature or temperature difference due to the simultaneous modification of supersaturation rate, temperature polarisation and concentration polarisation. An increase in supersaturation rate reduced induction time and increased supersaturation at induction. This increased nucleation rate and was complemented by a reduction in scaling. While this conforms with classical nucleation theory, it contradicts recommendations in the literature, which generally advocate for operation within a region of low supersaturation. This was explained by the modification of the supersaturation rate independent of boundary layer characteristics which resulted in a comparable supersaturated state within the bulk and boundary layer once supersaturation rate was increased and is a critical foundation for the development of scaling mitigation strategies. Two discrete regions for primary nucleation were described to discriminate between heterogeneous and homogeneous nucleation mechanisms and their physical relevance confirmed through characterisation of the scale deposit formed within each domain. Crystal growth could be described within the scale deposit and bulk crystal phase and related to the local supersaturation, which also informed on crystal size. While further work is required to confirm, the physical characteristics of the crystal phase within the bulk solution appear distinct from those within the scale deposit, which would indicate that the mechanisms of scale formation and of bulk crystal formation may be phenomenologically distinct. This may be facilitated by temporal examination of the crystal phase in the bulk solution, complemented by the direct measurement of supersaturation, to ensure the growth profile can be related explicitly to the metastable zone width.

Membrane distillation is a contemporary solution for evaporative crystallisation where poor regulation of nucleation is common in conventional evaporators as mixing is generally in a discrete domain of the mass transfer zone, while the decoupling of heat and mass transfer have also made crystal growth difficult to control. This study evidences that with control of heat and mass transfer over a well-defined surface area, nucleation rate and crystal growth can be regulated and in a scalable platform technology. High solubility salts are most likely to initiate adhesive growth due to their greater dependency on heterogeneous primary nucleation. However, membrane area-to-volume ratio has been demonstrated to mitigate scaling by sodium chloride, which evidences membrane distillation as a valid option for zero liquid discharge of desalination brines. The increase in crystal size with nucleation rate is a seemingly unique facet of this configuration and is likely a function of the two discrete regions of supersaturation that are initiated. Importantly, this provides an enhanced capability for crystal growth control in evaporative crystallisers, which are ordinarily limited to regulation by simple temperature setpoint. Although an increase in hollow-fibre membrane area also increased packing density to a commercially relevant fractional volume, less scaling (by adhesion or deposition) was observed at higher membrane areas. We therefore propose that it may be possible to translate similar operation to a wider set of membrane configurations (e.g. spiral wound) characterised by narrow channels without incurring substantive risk based on this work, provided kinetic modification of the supersaturation is facilitated to preference a homogeneous primary nucleation pathway.

Author statement

A. Ouda: Conceptualization; Data curation; Formal analysis; Investigation; Methodology; Roles/Writing - original draft;

Y. Bajón Fernández: Writing - review & editing.

E. McAdam: Conceptualization; Data curation; Formal analysis; Funding acquisition; Investigation; Methodology; Project administration; Supervision; Writing - review & editing.

Declaration of competing interest

The authors declare that they have no known competing financial interests or personal relationships that could have appeared to influence the work reported in this paper.

Data availability

A link to the data will be provided upon completion of peer review

Acknowledgements

This research was financially supported by European Research Council Starting Grant, ‘Sustainable chemical alternatives for reuse in

the circular economy' (StG, SCARCE, 714080). The data underlying this paper can be accessed through the following https://doi.org/10.17862/cranfield.rd.22775144.

Nomenclature and abbreviations

N	permeate flux, kg m^{-2} h^{-1}
L	hollow fibre length, m
A	effective membrane area, m^2
m	mass of permeate kg
Q	heat transfer, W m^{-2}
Qv	latent heat of evaporation, W m^{-2}
Qc	conductive heat flux through the membrane, W m^{-2}
k_m	membrane thermal conductivity, W m^{-1} K^{-1}
k_p	polymer thermal conductivity, W m^{-1} K^{-1}
k_g	air thermal conductivity, W m^{-1} K^{-1}
k_f	thermal conductivity of feed, W m^{-1} K^{-1}
k_p	thermal conductivity of permeate, W m^{-1} K^{-1}
T_{fm}	feed temperature adjacent to membrane surface, K
T_{pm}	permeate temperature adjacent to membrane surface, K
T_f	bulk temperature in feed, k
T_p	bulk temperature in permeate, k
d_i	outer diameter, mm
d_o	outer diameter, mm
d_{hf}	hydraulic diameter of feed flow channel
d_{hp}	hydraulic diameter of permeate flow channel
$H_{V,T}$	vapour latent heat, KJ kg^{-1}
h_m	heat transfer coefficient of the membrane, W m^{-2} K^{-1}
h_v	heat transfer coefficient of vapour, W m^{-2} K^{-1}
h_f	film heat transfer coefficients associated of feed side, W m^{-2} K^{-1}
h_p	film heat transfer coefficients associated of permeate side, W m^{-2} K^{-1}
Nu	Nusselt's number
Re	Reynold's number, dimensionless
Pr	Prandtl's number, dimensionless
v	velocity, m s^{-1}
c_p	specific heat of feed/permeate, J kg^{-1} K^{-1}
C_{fm}	interfacial concentration close to the membrane surface, g $_{NaCl}$ g^{-1} $_{solution}$
C_{fb}	feed bulk concentration, g $_{NaCl}$ g^{-1} $_{solution}$
k_s	solute mass transfer coefficient, m s^{-1}
Sh	Sherwood number, dimensionless
Sc	Schmidt number, dimensionless
J	nucleation rate, No. m^{-3} s^{-1}
ΔG^*	Gibb's free energy, kJ mol^{-1}
t_{ind}	induction time
k_B	Boltzmann constant, 1.38 x 10^{-23} J K^{-1}
v_o	molecular volume, m^3
M	molar weight, kg mol^{-1}
ρ_{cry}	crystal density, kg m^{-3}
N_a	Avogadro's number (6.022 x 10^{23} molecules mol^{-1})
T	nucleation temperature, K
A	pre-exponential parameter, m^{-3} s^{-1}
B	thermodynamic parameter for nucleation
$\Delta C_{max.fm}$	maximum MSZW at membrane surface, mg g^{-1} solution
R'	concentrating rate, g 100 g^{-1} solution h^{-1}
F_p	permeate flow rate, kg h^{-1}
k	nucleation rate constant, No. m^{-3-n} s^{-1+n}
n	nucleation order, dimensionless

Greek letters

δ_m	membrane thickness, m
ε	membrane porosity, %
ρ	density, kg m^{-3}
μ	viscosity, Pa s^{-1}
γ	interfacial energy, mJ m^{-2}
θ	contact angle, °

Appendix

Nusselt number, Reynold number and Prandtl number were calculated using the following equations:

$$Nu = 1.86\left(Re\ \mathrm{Pr}\ d_h/L\right)^{0.33} \tag{A1}$$

$$Re = \frac{d_h\ V\ \rho}{\mu} \tag{A2}$$

$$Pr = \frac{C_p \mu}{k} \tag{A3}$$

where v, ρ, μ and c_p are the velocity (m s^{-1}), density (kg m^{-3}), viscosity (Pa s^{-1}) and specific heat of feed/permeate (J kg^{-1} K^{-1}) respectively and L (m) is the hollow fibre length. The solute mass transfer coefficient k_s (m s^{-1}) is estimated using the following equations:

$$\frac{Sh_f}{Sc_f^{0.33}} = \frac{Nu_f}{Pr_f^{0.33}} \tag{A4}$$

where Sherwood (Sh) and Schmidt (Sc):

$$Sh_f = \frac{k_s D_h}{D_s} \tag{A5}$$

$$Sc_f = \frac{\mu_f}{P_f D_s} \tag{A6}$$

The growth rate can be calculated according to classical nucleation theory as follows:

$$G = K_G\ (\mathrm{c} - \mathrm{c}*)^{\mathrm{g}} \tag{A7}$$

$$\log\ (G) = \log\ (K_G) + g\ \log\ (c - c*) \tag{A8}$$

where K_G is the kinetic rate constant, (c-c*) is the growth driving force, c ($g_{\ NaCl}\ g^{-1}_{\ solution}$) is the feed bulk concentration and c* ($g_{\ NaCl}\ g^{-1}_{\ solution}$) is the solubility. Linearisation of the relationship between log(G) and log(c-c*), yields (g) as the gradient of the curve and $\log\ (K_G)$ as intercept.

References

[1] Q. Chen, M. Burhan, M.W. Shahzad, D. Ybyraiymkul, F.H. Akhtar, Y. Li, K.C. Ng, A zero liquid discharge system integrating multi-effect distillation and evaporative crystallization for desalination brine treatment, Desalination 502 (2021), 114928, https://doi.org/10.1016/j.desal.2020.114928.

[2] M.C. Sparenberg, I. Ruiz Salmón, P. Luis, Economic evaluation of salt recovery from wastewater via membrane distillation-crystallization, Separ. Purif. Technol. 235 (2020), 116075, https://doi.org/10.1016/j.seppur.2019.116075. April 2019.

[3] A. Jones, S. Rigopoulos, R. Zauner, Crystallization and precipitation engineering, Comput. Chem. Eng. 29 (2005) 1159–1166, https://doi.org/10.1016/j.compchemeng.2005.02.022, 6 SPEC. ISS.

[4] A.V. Mohod, P.R. Gogate, Improved crystallization of ammonium sulphate using ultrasound assisted approach with comparison with the conventional approach, Ultrason. Sonochem. 41 (May 2017) (2018) 310–318, https://doi.org/10.1016/j.ultsonch.2017.09.047.

[5] J. Ulrich, P. Frohberg, Problems, potentials and future of industrial crystallization, Front. Chem. Sci. Eng. 7 (1) (2013) 1–8, https://doi.org/10.1007/s11705-013-1304-y.

[6] E. Chabanon, D. Mangin, C. Charcosset, Membranes and crystallization processes: state of the art and prospects, J. Membr. Sci. 509 (2016) 57–67, https://doi.org/10.1016/j.memsci.2016.02.051.

[7] G. Di Profio, E. Curcio, E. Drioli, Supersaturation control and heterogeneous nucleation in membrane crystallizers: facts and perspectives, Ind. Eng. Chem. Res. 49 (23) (2010) 11878–11889, https://doi.org/10.1021/ie100418z.

[8] X. Jiang, X. Ruan, W. Xiao, D. Lu, G. He, A novel membrane distillation response technology for nucleation detection, metastable zone width measurement and analysis, Chem. Eng. Sci. 134 (2015) 671–680, https://doi.org/10.1016/j.ces.2015.05.030.

[9] X. Jiang, L. Tuo, D. Lu, B. Hou, W. Chen, G. He, Progress in membrane distillation crystallization: process models, crystallization control and innovative applications, Front. Chem. Sci. Eng. 11 (4) (2017) 647–662, https://doi.org/10.1007/s11705-017-1649-8.

[10] I. Ruiz Salmón, P. Luis, Membrane crystallization via membrane distillation, Chem. Eng. Process: Process Intensif. 123 (2018) 258–271, https://doi.org/10.1016/j.cep.2017.11.017. November 2017.

[11] Y. Choi, G. Naidu, L.D. Nghiem, S. Lee, S. Vigneswaran, Membrane distillation crystallization for brine mining and zero liquid discharge: opportunities, challenges, and recent progress, Environ. Sci.: Water Research and Technology 5 (7) (2019) 1202–1221, https://doi.org/10.1039/c9ew00157c.

[12] H. Elcik, L. Fortunato, A. Alpatova, S. Soukane, J. Orfi, E. Ali, H. AlAnsary, T. O. Leiknes, N. Ghaffour, Multi-effect distillation brine treatment by membrane distillation: effect of antiscalant and antifoaming agents on membrane performance and scaling control, Desalination 493 (July) (2020), https://doi.org/10.1016/j.desal.2020.114653.

[13] M. Gryta, Fouling in direct contact membrane distillation process, J. Membr. Sci. 325 (1) (2008) 383–394, https://doi.org/10.1016/j.memsci.2008.08.001.

[14] A. Ali, C.A. Quist-Jensen, F. Macedonio, E. Drioli, Application of membrane crystallization for minerals' recovery from produced water, Membranes 5 (4) (2015) 772–792, https://doi.org/10.3390/membranes5040772.

[15] F. Edwie, T.S. Chung, Development of simultaneous membrane distillation-crystallization (SMDC) technology for treatment of saturated brine, Chem. Eng. Sci. 98 (2013) 160–172, https://doi.org/10.1016/j.ces.2013.05.008.

[16] G. Naidu, S. Jeong, S. Vigneswaran, Influence of feed/permeate velocity on scaling development in a direct contact membrane distillation, Separ. Purif. Technol. 125 (2014) 291–300, https://doi.org/10.1016/j.seppur.2014.01.049.

[17] T. Horseman, Y. Yin, K.S. Christie, Z. Wang, T. Tong, S. Lin, Wetting, scaling, and fouling in membrane distillation: state-of-the-art insights on fundamental mechanisms and mitigation strategies, ACS ES&T Engineering 1 (1) (2021) 117–140, https://doi.org/10.1021/acsestengg.0c00025.

[18] K. Sangwal, On the interpretation of metastable zone width in anti-solvent crystallization, Cryst. Res. Technol. 45 (9) (2010) 909–919, https://doi.org/10.1002/crat.201000319.

[19] C. Bian, H. Chen, X. Song, J. Yu, Metastable zone width and the primary nucleation kinetics for cooling crystallization of NaNO3 from NaCl-NaNO3-H2O system, J. Cryst. Growth 518 (2019) 5–13, https://doi.org/10.1016/j.jcrysgro.2019.04.013. December 2018.

[20] G. Di Profio, S. Tucci, E. Curcio, E. Drioli, Controlling polymorphism with membrane-based crystallizers: application to form i and II of paracetamol, Chem. Mater. 19 (10) (2007) 2386–2388, https://doi.org/10.1021/cm0701005.

[21] L. Zhou, Z. Wang, M. Zhang, M. Guo, S. Xu, Q. Yin, Determination of metastable zone and induction time of analgin for cooling crystallization, Chin. J. Chem. Eng. 25 (3) (2017) 313–318, https://doi.org/10.1016/j.cjche.2016.05.046.

[22] M. Lenka, D. Sarkar, Determination of metastable zone width, induction period and primary nucleation kinetics for cooling crystallization of L-asparaginenohydrate, J. Cryst. Growth 408 (2014) 85–90, https://doi.org/10.1016/j.jcrysgro.2014.09.027.

[23] T. Tong, A.F. Wallace, S. Zhao, Z. Wang, Mineral scaling in membrane desalination: mechanisms, mitigation strategies, and feasibility of scaling-resistant membranes,

J. Membr. Sci. 579 (February) (2019) 52–69, https://doi.org/10.1016/j.memsci.2019.02.049.
[24] J. Kim, J. Kim, S. Hong, Recovery of water and minerals from shale gas produced water by membrane distillation crystallization, Water Res. 129 (2018) 447–459, https://doi.org/10.1016/j.watres.2017.11.017.
[25] L.D. Tijing, Y.C. Woo, J.S. Choi, S. Lee, S.H. Kim, H.K. Shon, Fouling and its control in membrane distillation-A review, J. Membr. Sci. 475 (2015) 215–244, https://doi.org/10.1016/j.memsci.2014.09.042.
[26] M.T. Chan, A.G. Fane, J.T. Matheickal, R. Sheikholeslami, Membrane distillation crystallization of concentrated salts - flux and crystal formation, J. Membr. Sci. 257 (1–2) (2005) 144–155, https://doi.org/10.1016/j.memsci.2004.09.051.
[27] J. Nývlt, Kinetics of nucleation in solutions, J. Cryst. Growth 3–4 (1968) 377–383, https://doi.org/10.1016/0022-0248(68)90179-6.
[28] K. Sangwal, A novel self-consistent Nývlt-like equation for metastable zone width determined by the polythermal method, Cryst. Res. Technol. 44 (3) (2009) 231–247, https://doi.org/10.1002/crat.200800501.
[29] M.C. Sparenberg, S. Chergaoui, V. Sang Sefidi, P. Luis, Crystallization control via membrane distillation-crystallization: a review, Desalination 519 (June 2021) (2022), 115315, https://doi.org/10.1016/j.desal.2021.115315.
[30] X. Yang, R. Wang, L. Shi, A.G. Fane, M. Debowski, Performance improvement of PVDF hollow fiber-based membrane distillation process, J. Membr. Sci. 369 (1–2) (2011) 437–447, https://doi.org/10.1016/j.memsci.2010.12.020.
[31] A. Ali, J.H. Tsai, K.L. Tung, E. Drioli, F. Macedonio, Designing and optimization of continuous direct contact membrane distillation process, Desalination 426 (2018) 97–107, https://doi.org/10.1016/j.desal.2017.10.041. October 2017.
[32] J. Phattaranawik, R. Jiraratananon, A.G. Fane, Heat transport and membrane distillation coefficients in direct contact membrane distillation, J. Membr. Sci. 212 (1–2) (2003) 177–193, https://doi.org/10.1016/S0376-7388(02)00498-2.
[33] G. Chen, Y. Lu, X. Yang, R. Wang, A.G. Fane, Quantitative study on crystallization-induced scaling in high-concentration direct-contact membrane distillation, Ind. Eng. Chem. Res. 53 (40) (2014) 15656–15666, https://doi.org/10.1021/ie501610q.
[34] M.C. García-Payo, M.A. Izquierdo-Gil, C. Fernández-Pineda, Air gap membrane distillation of aqueous alcohol solutions, J. Membr. Sci. 169 (1) (2000) 61–80, https://doi.org/10.1016/S0376-7388(99)00326-9.
[35] S. Wang, M. Feng, H. Du, J.J. Weigand, Y. Zhang, X. Wang, Determination of metastable zone width, induction time and primary nucleation kinetics for cooling crystallization of sodium orthovanadate from NaOH solution, J. Cryst. Growth 545 (May) (2020), 125721, https://doi.org/10.1016/j.jcrysgro.2020.125721.
[36] F. Zou, W. Zhuang, J. Wu, J. Zhou, P.P. Yang, Q. Liu, Y. Chen, H. Ying, Determination of metastable zone widths and the primary nucleation and growth mechanisms for the crystallization of disodium guanosine 5′-monophosphate from a water-ethanol system, Ind. Eng. Chem. Res. 54 (1) (2015) 137–145, https://doi.org/10.1021/ie504035j.
[37] S. Karthika, T.K. Radhakrishnan, P. Kalaichelvi, Measurement of nucleation rate of ibuprofen in ionic liquid using induction time method, J. Cryst. Growth 521 (May) (2019) 55–59, https://doi.org/10.1016/j.jcrysgro.2019.06.004.
[38] K. Sangwal, E. Mielniczek-Brzóska, S. Barylska, Solubility of ammonium oxalate in water-acetone mixtures and metastable zone width of their solutions, Chem. Eng. Res. Des. 92 (3) (2014) 491–499, https://doi.org/10.1016/j.cherd.2013.08.031.
[39] R. Thanedgunbaworn, R. Jiraratananon, M.H. Nguyen, Shell-side mass transfer of hollow fibre modules in osmotic distillation process, J. Membr. Sci. 290 (1–2) (2007) 105–113, https://doi.org/10.1016/j.memsci.2006.12.021.
[40] A. Alkhudhiri, N. Darwish, N. Hilal, Membrane distillation: a comprehensive review, Desalination 287 (2012) 2–18, https://doi.org/10.1016/j.desal.2011.08.027.
[41] L. Martínez, Comparison of membrane distillation performance using different feeds, Desalination 168 (1–3) (2004) 359–365, https://doi.org/10.1016/j.desal.2004.07.022.
[42] J.W. Mullin, *Crystallisation* (Fourth), 2001.
[43] G. Zeng, H. Li, S. Huang, X. Wang, J. Chen, Determination of metastable zone width and the primary nucleation kinetics of sodium sulfate, Theor. Found. Chem. Eng. 49 (6) (2015) 869–876, https://doi.org/10.1134/S0040579515050309.
[44] F. Edwie, T.S. Chung, Development of hollow fiber membranes for water and salt recovery from highly concentrated brine via direct contact membrane distillation and crystallization, J. Membr. Sci. (2012), https://doi.org/10.1016/j.memsci.2012.07.001.
[45] M. Lenka, D. Sarkar, Determination of metastable zone width and nucleation kinetics for combined cooling and antisolvent crystallization of L-asparagine monohydrate in water-isopropanol mixture, J. Cryst. Growth 501 (August) (2018) 66–73, https://doi.org/10.1016/j.jcrysgro.2018.08.031.
[46] H. Kurokawa, T. Sawa, Heat recovery characteristics of membrane distillation, Heat Tran. Jpn. Res. 25 (3) (1996) 135–150, https://doi.org/10.1002/(SICI)1520-6556(1996)25:3<135::AID-HTJ1>3.0.CO;2-Y.
[47] M. Khayet, Membranes and theoretical modeling of membrane distillation: a review, Adv. Colloid Interface Sci. 164 (1–2) (2011) 56–88, https://doi.org/10.1016/j.cis.2010.09.005.
[48] W. Omar, J. Ulrich, Determination of nucleation parameters and the solid liquid interfacial energy of the KCl-ethanol-water system, Cryst. Res. Technol. 42 (5) (2007) 432–439, https://doi.org/10.1002/crat.200610843.
[49] X. Ni, A. Liao, Effects of cooling rate and solution concentration on solution crystallization of L-glutamic acid in an oscillatory baffled crystallizer, Cryst. Growth Des. 8 (8) (2008) 2875–2881, https://doi.org/10.1021/cg7012039.
[50] S. Datta, D.J.W. Grant, Effect of supersaturation on the crystallization of phenylbutazone polymorphs, Cryst. Res. Technol. 40 (3) (2005) 233–242, https://doi.org/10.1002/crat.200410331.
[51] Y. Liu, T. Horseman, Z. Wang, H.A. Arafat, H. Yin, S. Lin, T. He, Negative pressure membrane distillation for excellent gypsum scaling resistance and flux enhancement, Environ. Sci. Technol. 56 (2) (2022) 1405–1412, https://doi.org/10.1021/acs.est.1c07144.
[52] J. Desarnaud, H. Derluyn, J. Carmeliet, D. Bonn, N. Shahidzadeh, Hopper growth of salt crystals, J. Phys. Chem. Lett. 9 (11) (2018) 2961–2966, https://doi.org/10.1021/acs.jpclett.8b01082.
[53] S. Teychené, B. Biscans, Nucleation kinetics of polymorphs: induction period and interfacial energy measurements, Cryst. Growth Des. 8 (4) (2008) 1133–1139, https://doi.org/10.1021/cg0609320.
[54] T. Tong, A.F. Wallace, S. Zhao, Z. Wang, Mineral scaling in membrane desalination: mechanisms, mitigation strategies, and feasibility of scaling-resistant membranes, J. Membr. Sci. 579 (January) (2019) 52–69, https://doi.org/10.1016/j.memsci.2019.02.049.
[55] T. Horseman, C. Su, K.S.S. Christie, S. Lin, Highly effective scaling mitigation in membrane distillation using a superhydrophobic membrane with gas purging, Environ. Sci. Technol. Lett. 6 (7) (2019) 423–429, https://doi.org/10.1021/acs.estlett.9b00354.
[56] X. Jiang, Y. Niu, S. Du, G. He, Membrane crystallization: engineering the crystallization via microscale interfacial technology, Chem. Eng. Res. Des. 178 (2022) 454–465, https://doi.org/10.1016/j.cherd.2021.12.042.
[57] H. Jin, H. Athreya, S. Wang, K. Nawaz, Experimental study of crystallization fouling by calcium carbonate : effects of surface structure and material, Desalination 532 (December 2021) (2022), 115754, https://doi.org/10.1016/j.desal.2022.115754.
[58] I.V. Alexandrova, A.A. Ivanov, D.V. Alexandrov, How the intermediate stage of a phase transition process transforms to the concluding stage of Ostwald ripening, J. Cryst. Growth 532 (2020), 125456, https://doi.org/10.1016/j.jcrysgro.2019.125456. December 2019.
[59] A.S. Myerson, D. Erdemir, A.Y. Lee, Handbook of Industrial Crystallization, third ed., Cambridge University Press, 2019 https://doi.org/10.1017/9781139026949.
[60] M.A. Lovette, A.R. Browning, D.W. Griffin, J.P. Sizemore, R.C. Snyder, M. F. Doherty, Crystal shape engineering, Ind. Eng. Chem. Res. 47 (24) (2008) 9812–9833, https://doi.org/10.1021/ie800900f.



https://dspace.org/

Modifying supersaturation rate with membrane area to volume ratio: scaling reduction and improved crystal growth control in membrane distillation crystallisation

Ouda, Alaa Samir; Bajón Fernández, Yadira; McAdam, Ewan

2023-10-05
Elsevier
https://doi.org/10.1016/j.memsci.2023.121838
Ouda A, Fernández YB, McAdam E. (2023) Modifying supersaturation rate with membrane area to volume ratio: scaling reduction and improved crystal growth control in membrane distillation crystallisation. Journal of Membrane Science, Volume 683, October 2023, Article number 121838

Downloaded from a DSpace repository. https://dspace.org/